MOF-Derived In$_2$O$_3$/CuO p-n Heterojunction Photoanode Incorporating Graphene Nanoribbons for Solar Hydrogen Generation

Li Shi, Daniele Benetti,* Qin Wei,* and Federico Rosei*

Solar-driven photoelectrochemical (PEC) water splitting is a promising approach toward sustainable hydrogen (H$_2$) generation. However, the design and synthesis of efficient semiconductor photocatalysts via a facile method remains a significant challenge, especially p-n heterojunctions based on composite metal oxides. Herein, a MOF-on-MOF (metal-organic framework) template is employed as the precursor to synthesize In$_2$O$_3$/CuO p-n heterojunction composite. After incorporation of small amounts of graphene nanoribbons (GNRs), the optimized PEC devices exhibited a maximum current density of 1.51 mA cm^{-2} (at 1.6 V vs RHE) under one sun illumination (AM 1.5G, 100 mW cm^{-2}), which is approximately four times higher than that of the reference device based on only In$_2$O$_3$ photoanodes. The improvement in the performance of these hybrid anodes is attributed to the presence of a p-n heterojunction that enhances the separation efficiency of photogenerated electron-hole pairs and suppresses charge recombination, as well as the presence of GNRs that can increase the conductivity by offering better path for electron transport, thus reducing the charge transfer resistance. The proposed MOF-derived In$_2$O$_3$/CuO p-n heterojunction composite is used to demonstrate a high-performance PEC device for hydrogen generation.

1. Introduction

The rapid growth in energy demand together with the excessive use of fossil fuels and resulting environmental pollution

L. Shi, D. Benetti, F. Rosei
Centre for Energy
Materials and Telecommunications
Institut National de la Recherche Scientifique
1650 Boul. Lionel-Boulet, Varennes QC J3×1P7, Canada
E-mail: daniele.benetti@inrs.ca; rosei@emt.inrs.ca
L. Shi, Q. Wei
Key Laboratory of Interfacial Reaction & Sensing Analysis in Universities of Shandong
School of Chemistry and Chemical Engineering
University of Jinan
Jinan 250022, P. R. China
E-mail: chm_weiq@ujn.edu.cn

have led to the urgent need to develop renewable energy solutions.[1] Solar fuels such as Hydrogen (H$_2$), offer the potential to produce clean power from a renewable source.[2] Among different types of solar H$_2$ generation systems, photoelectrochemical (PEC) water splitting presents several advantages such as high theoretical efficiency (up to >30%), low cost, and eco-friendliness.[3] To obtain a high solar-to-hydrogen (STH) efficiency in such systems, it is crucial to design long-term stable, low-cost, and high-performance photoelectrocatalysts.[4]

Indium oxide (In$_2$O$_3$), an n-type semiconductor, stands out as a promising material for PEC applications due to the suitable position of its conduction and valence bands for water splitting, good conductivity, and high stability in corrosive environments.[5] However, the high recombination rate of photogenerated electron-hole pairs in pure In$_2$O$_3$ reduces its catalytic activity and H$_2$ yield.[6] To achieve higher STH in In$_2$O$_3$ photoelectrocatalysts, it is thus essential to suppress charge recombination. Several techniques can be effective in enhancing the properties of metal oxide photoelectrodes, including surface functionalization, doping, and heterojunctions formation.[7] Among these strategies, composite semiconductors with a p-n heterojunction structure offer an interesting solution to reduce the recombination rate of photogenerated carriers while broadening the light absorption range.[8] Several p-type materials are considered promising for building p-n junctions for PEC applications, including p-Si, NiO, CuO, and III–V group p-type semiconductors (e.g., p-GaN, InP, and GaAs).[9] Among these, copper oxide (CuO) presents several attractive properties such as relative abundance, low cost, narrow bandgap (1.4-2.3 eV), low toxicity, high light absorption coefficient, and a high activity for photocatalytic water splitting.[10] It has been shown that In$_2$O$_3$/CuO with p-n heterojunction can improve the separation efficiency of photogenerated electron/hole pairs, yielding excellent photocatalytic H$_2$ production.[8] However, In$_2$O$_3$/CuO composites are traditionally prepared by wet chemical methods (e.g., hydrothermal synthesis),[11] which do not allow to easily control the properties of the final materials in a scalable manner, while maintaining a high degree of reproducibility.[12] Hence, developing a simple synthesis

**ADVANCED
SCIENCE NEWS**
www.advancedsciencenews.com

**NANO · MICRO
small**
www.small-journal.com

procedure that meets all the requirements is highly desirable yet challenging.

Templating by metal-organic frameworks (MOFs) is an emerging approach to synthesize metal oxides composite with optimized properties.[3,13] The structure of MOFs can be adjusted at the molecular level by reasonably selecting various species of metals and organic linkers.[14] When a MOF-on-MOF heterostructure is used as precursor, it is possible to achieve a final uniform contact between two different metal oxides.[15] Based on this design philosophy, in this work, two different MOFs, Cu-BDC (Cu-based MOFs) and MIL-68(In-based MOF) have been selected as optimal templates for obtaining a In_2O_3/CuO p-n heterojunction composite. In particular, Cu-BDC is grown on the surface of hexagonal rod-shaped MIL-68(In) to form MIL-68(In)/Cu-BDC heterostructure. After annealing, the hybrid can form a In_2O_3/CuO p-n heterojunction composite, while retaining the original MOF hollow hexagonal rod-shaped structure.

In parallel, considerable efforts have focused on the incorporation of low-dimensional (1D) carbon allotrope nanostructures into semiconductor electrodes to enhance the charge transport and collection,[16] such as carbon nanotubes (CNTs),[17] graphene,[18] and graphene oxide.[19] Graphene nanoribbons (GNRs), a quasi-1-D nanoribbon carbon allotrope structure, have been already employed with success in a wide range of optoelectronic devices.[20] In this way, by adding a controlled amount of GNRs, the charge transport efficiency can be increased by enabling better electron transport. However, to the best of our knowledge, there is no report on the application of GNRs in In_2O_3/CuO p-n heterojunction for PEC devices.

Herein, we developed a facile synthesis of p-n heterojunction In_2O_3/CuO composites with hollow hexagonal rod-shaped structure by using MOF-on-MOF as a sacrificial template. By incorporating specific amounts of GNRs in the In_2O_3/CuO (In_2O_3/CuO-GNRs) photoanode, the synthesized material shows an enhanced efficiency for PEC H_2 generation. In particular, the optimized device based on the In_2O_3/CuO-GNRs photoanode exhibited a remarkable photocurrent density of 1.51 mA cm^{-2} at 1.6 V versus RHE under one sun illumination (AM 1.5 G, 100 mW cm^{-2}), which is 70% higher than the device based on In_2O_3/CuO photoanodes without GNRs (0.89 mA cm^{-2}). In addition, In_2O_3/CuO-GNRs samples show good long-term stability in NaOH solution without obvious degradation, benefiting from the protection offered by the p-n heterojunction. The role of the In_2O_3/CuO composite in charge transfer and band energy alignment was determined by electrochemical impedance spectroscopy (EIS), X-ray photoelectron

spectroscopy (XPS), ultraviolet photoelectron spectroscopy (UPS) and differential reflectance spectroscopy (DRS). We also discuss the mechanisms underlying the formation of p-n junctions and the separation of photogenerated electrons and holes.
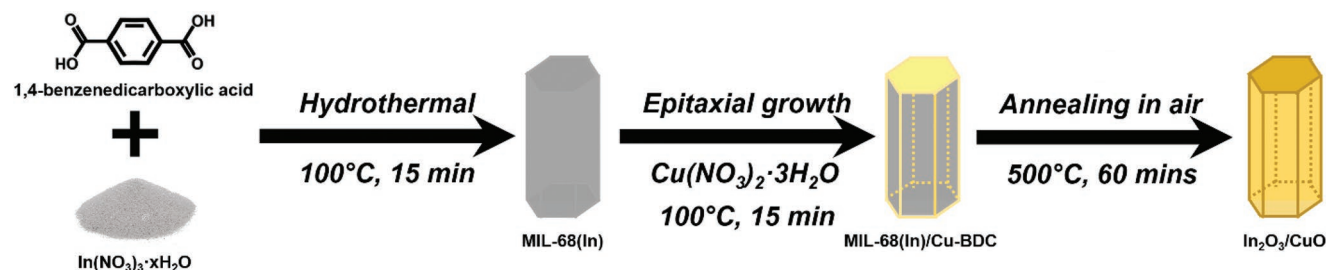
2. Results and Discussion

2.1. Synthesis and Structural Characterization

The synthesis procedure to obtain hollow hexagonal rod-shaped In_2O_3/CuO composites is schematically depicted in **Scheme 1**. First, a well-defined In-based MOF (MIL-68(In)) with hexagonal rod-shaped morphology is synthesized via a simple solvothermal reaction. The obtained MIL-68(In) is then dispersed in DMF solution (18 mL) with a copper precursor (copper nitrate hexahydrate) and annealed at 100 °C for 15 min. In this way, Cu-based MOFs (Cu-BDC) can be grown epitaxially on the MIL-68(In) to form MIL-68-In/Cu-BDC template. In_2O_3/CuO composites can be then obtained by annealing treatment of the MIL-68(In)/Cu-BDC template in ambient air at 500 °C for 1 h.

For comparison, MIL-68(In), Cu-BDC, and their respective oxides, In_2O_3 and CuO were also prepared with similar procedures. The calcination process of MIL-68(In), Cu-BDC, and MIL-68(In)/Cu-BDC was investigated by thermogravimetric analysis (TGA) (Figure S1, Supporting Information). The weight of the MIL-68(In)/Cu-BDC loss ≈26 wt% from room temperature to 200 °C can be attributed to the removal of the absorbed methanol and DMF solvent, whereas the noteworthy weight loss (around 44.4 wt%) from temperature 400 to 487 °C is assigned to the decomposition of the MOF skeleton (Figure S1c, Supporting Information). Based on the TGA result, the pyrolysis temperature for the MIL-68(In)/Cu-BDC precursor was set to 500 °C with a heating rate of 5 °C min^{-1} for 1 h in the air atmosphere to have full oxidation and conversion of the as-prepared MIL-68(In)/Cu-BDC into the In_2O_3/CuO.

Power X-ray diffraction (XRD) was used to characterize MIL-68(In)/Cu-BDC (**Figure 1**a). The MOFs structure exhibits sharp diffraction peaks, with all peaks consistent with previous reports,[15,21] confirming the formation of the crystalline MOF-on-MOF structure. XRD was also employed to characterize the crystallinity of the CuO, In_2O_3, and In_2O_3/CuO (Figure 1b). The XRD pattern indicates that, after annealing, the obtained In_2O_3/CuO composite contains both CuO (JCPDS No. 41–0254) and In_2O_3 (JCPDS No. 44–1087) phases. Likewise, the Cu-BDC-derived CuO and MIL-68(In) derived In_2O_3 can be assigned to

Scheme 1. Schematic illustration of MOF-templated technique to obtain In_2O_3/CuO composites.

**ADVANCED
SCIENCE NEWS**

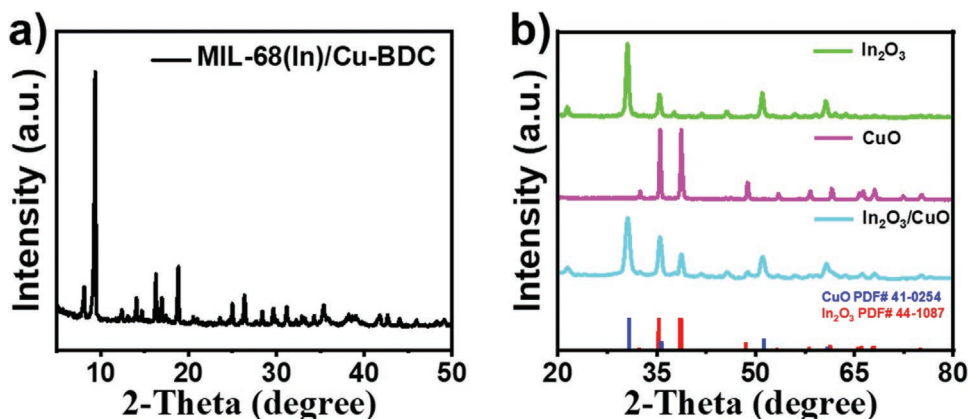www.advancedsciencenews.com

NANO · MICRO

small

www.small-journal.com

Figure 1. XRD patterns of a) MIL-68(In)/Cu-BDC precursor and that of b) In_2O_3 (green), CuO (magenta), and In_2O_3/CuO (cyan) (blue bar: monoclinic CuO, No. 41–0254; red bar: monoclinic In_2O_3, No.44-1087).

monoclinic CuO and In_2O_3.[22] No other peaks can be found in all three spectra, indicating the high purity of the products.

The morphologies and structure feature of In_2O_3/CuO were characterized by scanning electron microscopy (SEM), transmission electron microscopy (TEM), selected area electron diffraction (SAED), and high-angle annular dark-field scanning transmission electron microscopy (HAADF-STEM). The single MIL-68(In) (Figure S2, Supporting Information), shows a hexagonal rod-like morphology with average diameter and length of the rods of 2.5 and 7.8 μm, respectively. As observed in **Figure 2**a,b,c, the MIL-68(In)/Cu-BDC also displays a hexagonal rod-shaped morphology with a smooth surface. After calcination in ambient air, the In_2O_3/CuO composite retains the original hexagonal rod-shaped of MIL-68(In)/Cu-BDC (Figure S3, Supporting Information) and reveals a hierarchical hollow structure (Figure 2d) as visible by the difference in contrast in the TEM image. On the other hand, the surface of the calcined particles becomes rough. Figure S4, Supporting Information, displays the TEM and SAED pattern for the pure In_2O_3 derived by MIL-68(In) and pure CuO derived by Cu-BDC. As observed in TEM, the In_2O_3 retains the rod-like morphology after annealing, while CuO is amorphous. The SAED pattern of In_2O_3/CuO composite (Figure 1e) shows a group of diffraction rings which can be indexed to (211), (222), and (440) planes for In_2O_3, and (002), (111), and (202) planes for CuO. This result further validates the successful formation of the In_2O_3/CuO heterojunction. From the high-resolution TEM (HRTEM) image of In_2O_3/CuO composite (Figure 2f), it is possible to extract values of d-spacings of 2.92 Å and 2.52 Å that can be indexed to the (222) plane of In_2O_3 and (110) plane of CuO, respectively. Energy-dispersive X-ray spectroscopy (EDX) analysis (Figure S5, Supporting Information) confirms the presence of In, Cu, O, and elemental C in the In_2O_3/CuO composite. The elemental mapping images (Figure 2g–k) obtained in STEM mode clearly indicate relatively uniform distributions of In, Cu, O, and C elements.

The surface electronic properties and chemical states of the In_2O_3/CuO were analyzed by X-ray photoelectron spectroscopy (XPS) (**Figure 3**). The survey XPS spectra reveal the presence of In, Cu, and O peaks (Figure 3a), consistent with the EDX and XRD results. The C 1s peak, associated to adventitious

carbon in the environment, is also observed. The high-resolution XPS spectrum of O 1s (Figure 3b) can be deconvoluted into two major peaks, at 532.5 and 529.9 eV, assigned to the surface adsorbed oxygen groups (O–H bonds) and lattice oxygen (O_L), respectively.[8,11a] Likewise, the In 3d XPS spectrum (Figure 3c) shows two distinct peaks, which are attributed to the typical spin-orbit split In $3d_{5/2}$ (444.1 eV) and In $3d_{3/2}$ (451.6 eV), respectively. From these observations, we infer that In (III) is the dominating state in the product. When compared with the In 3d XPS spectrum of pure In_2O_3, In $3d_{5/2}$ (444.0 eV), the binding energies are slightly shifted, which is due to the occurrence of band bending in the In_2O_3/CuO composite (Figure S8e, Supporting Information and Figure 3c).[11a] The high-resolution XPS spectrum of Cu 2p (Figure 3d) exhibits two main peaks at 953.4 and 933.2 eV, corresponding to Cu $2p_{1/2}$ and Cu $2p_{3/2}$, respectively. The distance between these two peaks is around 20 eV, meaning a normal state of Cu^{2+}.[15] Additionally, the shake-up satellites (denoted as Sat.) at 940.6, 942.4, and 961.1 eV also suggest that the Cu atoms are in their +2 oxidation states, further confirming the presence of CuO. Therefore, by combining the various results from XRD, XPS, and TEM, it can be concluded that In_2O_3/CuO composites have been fabricated successfully.

2.2. Optical Properties and Band Alignment at the Heterojunction

Knowing the band edge positions of CuO and In_2O_3 and the band alignments is important to investigate the electron transfer process at the heterojunction. The combined analysis data from UV-DRS, UPS, and XPS can be used to determine the electronic band alignments.

The UV-DRS spectra of CuO, In_2O_3, and In_2O_3/CuO are shown in Figure S6, Supporting Information. All of them present absorption in the UV-vis region. The absorption edges for pure CuO, In_2O_3, and In_2O_3/CuO were ≈650, 460, and 550 nm, respectively. The In_2O_3/CuO-0.03% GNR was also tested with almost identical profiles, meaning that the presence of the GNR does not interfere with the optical properties of In_2O_3/CuO composite (Figure S6a, Supporting Information).
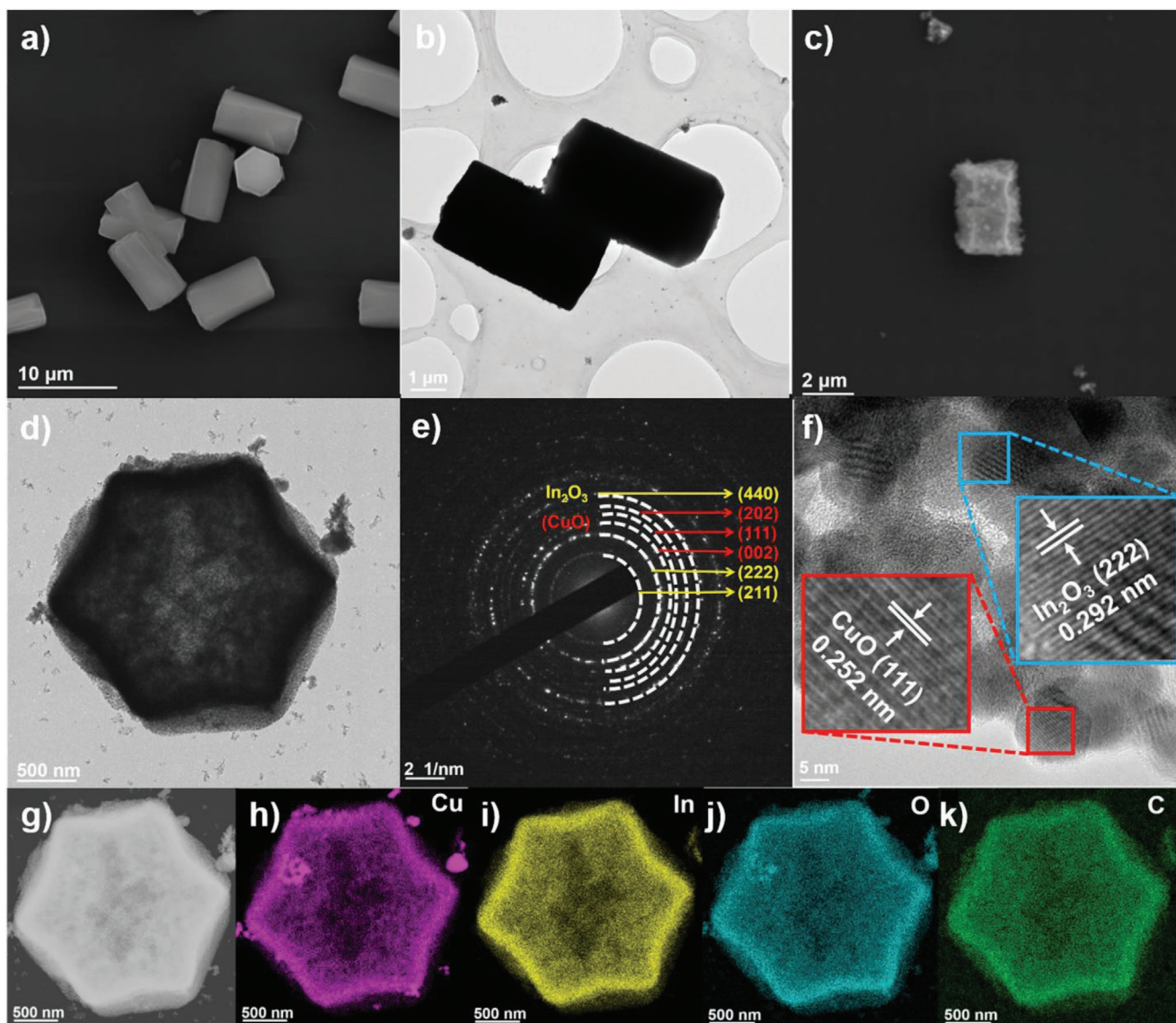
Figure 2. SEM a) and TEM b) images of the MIL-68(In)/Cu-BDC precursors. c) SEM images of In_2O_3/CuO. d) TEM images of In_2O_3/CuO e) SAED pattern of In_2O_3/CuO. f) HRTEM image of In_2O_3/CuO. g–k) HAADF-STEM image and corresponding EDX elemental mapping of In, Cu, O, and C elements for In_2O_3/CuO composite.

According to the classical Tauc's formula,[23] the optical bandgaps of $E_{BG}(CuO)$ and $E_{BG}(In_2O_3)$ are 1.79 and 2.70 eV, respectively (Figure S6b, Supporting Information). These values are consistent with previously reported values for CuO[22a,24] and In_2O_3.[25]

UPS with He I radiation (21.21 eV) was used to estimate the Fermi level (E_F) and valence band maximum (VBM) energy level.[26] Figure S7, Supporting Information shows the UPS spectra of CuO, In_2O_3, and In_2O_3/CuO, respectively. According to the linear intersection method, the E_{VBM} of CuO is calculated to be −5.62 eV (vs vacuum). Similarly, the work function and the corresponding E_F level of CuO are estimated to be 5.42 eV and −5.42 eV (vs vacuum), respectively. Since the value of $E_{BG}(CuO)$ is 1.79 eV, the conduction band minimum (E_{CBM}) is located at −3.83 eV (vs vacuum). According to the relationship between vacuum energy (E_{abs}) and the normal electrode potential (E^Θ),

$E_{abs} = −E^\Theta$ - 4.44 (at 298K)(pH = 0),[27] the corresponding relative valence and conduction band positions are +1.18 and −0.61 eV (vs NHE), respectively. Equally, the value of E_{VBM}, E_{CBM}, and E_F of In_2O_3 are +2.31, −0.39, and +0.2 eV (vs NHE), respectively (**Figure 4**a) (details in Supporting Information).

When the two metal oxides are in contact, a p-n heterojunction at the interface will be formed, and the new systems will attain equilibrium with a new Fermi level. At the same time, an interface depletion layer will be formed at the In_2O_3/CuO interface. The band offsets of the nanocomposite can be determined following the method of Kraut et al..[28] To accurately determine the valence band offset (ΔE_{VBO}), the energy difference between the core level (E_{CL}) and the valence band maximum (E_{VBM}) in the pure materials (all data are obtained from the corresponding XPS spectra), as well as the energy difference between the core levels at the interface of the heterostructure (ΔEInt CL)

**ADVANCED
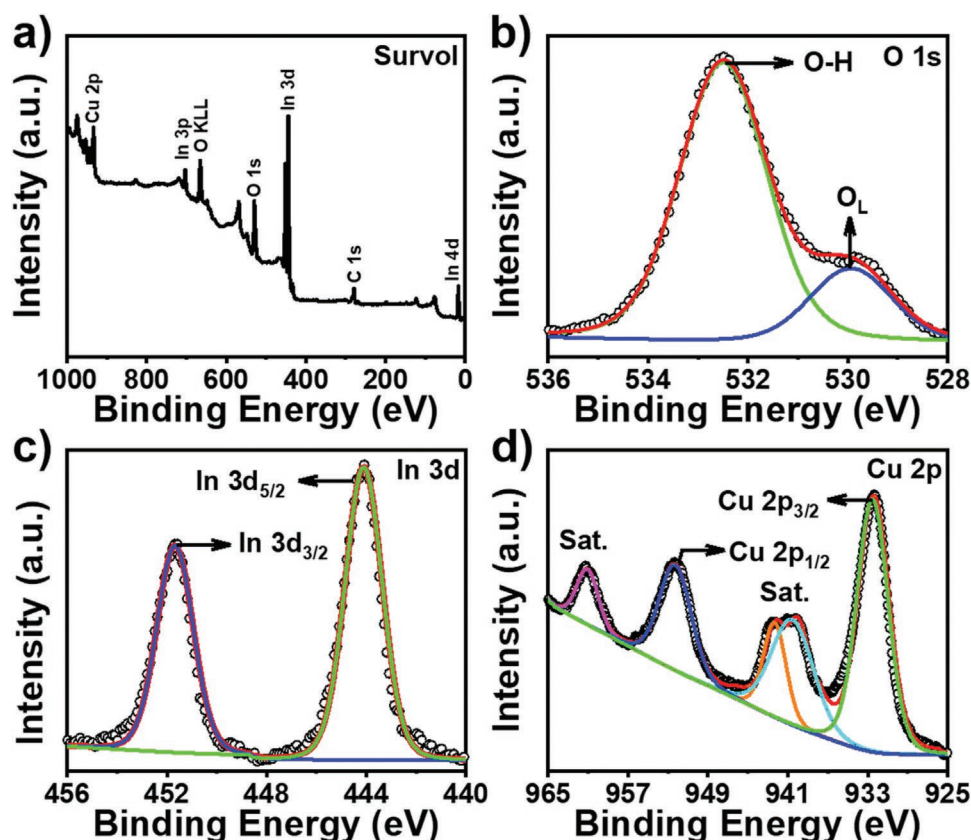SCIENCE NEWS**
www.advancedsciencenews.com

NANO · MICRO
small
www.small-journal.com

Figure 3. XPS survey spectra of a) In_2O_3/CuO. High-resolution O 1s spectra b). High-resolution In 3d spectra. c,d) High-resolution Cu 2p spectra.

are needed (Figure S8g–i in the Supporting Information provides the XPS spectra). Equations (1) and (2) are used to calculate ΔE_{VBO} and ΔEInt CL, respectively:[27]

$$\Delta E_{VBO} = \left(E_{CL}^{CuO} - E_{VBM}^{CuO} \right) - \left(E_{CL}^{In_2O_3} - E_{VBM}^{In_2O_3} \right) - \Delta E_{CL}^{Int} \qquad (1)$$

$$\Delta E_{CL}^{Int} = \left(E_{CL}^{CuO} - E_{CL}^{In_2O_3} \right)^{In_2O_3/CuO} \qquad (2)$$

The conduction band offset (ΔE_{CBO}) can be readily obtained from the bandgap energies (E_{BG}) of the pure materials and ΔE_{VBO} (Equations (3)):

$$\Delta E_{CBO} = E_{BG}^{CuO} - E_{BG}^{In_2O_3} + \Delta E_{VBO} \qquad (3)$$

Combining the information gathered during XPS and UV-DRS spectra indicates that for the In_2O_3/CuO nanocomposite $\Delta E_{VBO} = 1.03$ eV and $\Delta E_{CBO} = 0.12$ eV (Figure 4b). The energy difference between the conduction and valence bands for the materials in the In_2O_3/CuO nanocomposite are ≈0.10 eV higher in comparison with the values before contact. It is assumed that the difference value between E_{CBM} and E_F of In_2O_3 and D-value between E_{VBM} and E_F of CuO is kept constant before and after contact. Also, possible band bending is not taken into account.[29] Finally, the E_{VBM} of In_2O_3 in In_2O_3/CuO nanocomposite is calculated to be 1.46 eV (vs NHE), and the E_{CBM} of CuO in In_2O_3/CuO nanocomposite is calculated to be −0.78 eV (vs NHE). The obtained values are summarized in **Table 1**.

As shown in Figure 4b, the In_2O_3/CuO nanocomposite forms a Type II (staggered) band alignment heterostructure, whose highly energetic conduction band favors the separation of charges. Under light irradiation, photogenerated electrons from CuO can favorably transfer into the conduction band of In_2O_3, while photogenerated holes from In_2O_3 migrate into the valence band of CuO. The built-in electric field of In_2O_3/CuO p-n heterojunction facilitates carrier migration, enhancing the separation efficiency of photogenerated electron-hole pairs and suppressing charge recombination.

Mott–Schottky (M–S) tests were conducted to further confirm the semiconductor types of pristine of CuO, In_2O_3, and In_2O_3/CuO composite. The positive slope of the M–S plot confirms that the In_2O_3 is an n-type semiconductor (Figure S9a, Supporting Information),[30] and correspondingly, the negative slope demonstrates the typical p-type semiconductor property of CuO (Figure S9b, Supporting Information).[24] The Mott–Schottky plot of In_2O_3/CuO composite exhibits a typical inverted "V" shape, confirming the formation of a p-n heterojunction.[31]

2.3. PEC Measurements

To further improve the charge transfer in the photoanode, different contents of GNRs (0–0.05 wt%) were incorporated in the In_2O_3/CuO composite to build a PEC device. A bare In_2O_3/CuO composite was also used as reference. Figure S10, Supporting
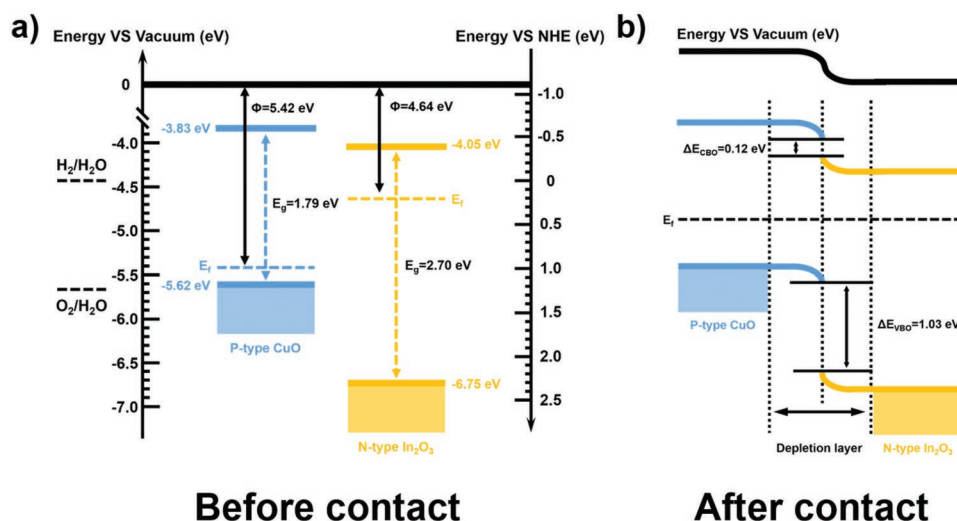
2300606 (5 of 10)

Figure 4. Energy band diagrams for a) CuO and In_2O_3 before contact and b) the energy band alignment of CuO/In_2O_3 heterojunction.

Information reports the Raman spectra of GNRs, In_2O_3/CuO, and the In_2O_3/CuO-GNRs photoanode. The Raman spectrum of pristine GNRs displays the characteristic D and G bands at 1347 cm^{-1} and 1578 cm^{-1} respectively, which are specific of the carbonaceous material.[17b,32] The In_2O_3/CuO-0.03 wt% GNRs film clearly shows the presence of D and G bands at 1340 and 1569 cm^{-1} respectively. This confirms the presence of GNRs in the In_2O_3/CuO-GNRs hybrid photoanode even after 30 min annealing at 500 °C under ambient conditions. However, the relative intensity of the D and G bands is lower, which may be due to the conformal coverage of GNRs by the In_2O_3/CuO composite and to the low concentration of GNRs (0.03 wt%) used. Moreover, the In_2O_3/CuO-GNRs hybrid photoanode was also analyzed via cross-section and plain-view SEM imaging corresponding to EDX (Figure S11, Supporting Information). The thickness of the In_2O_3/CuO-GNRs film is estimated to be ≈12.2 µm. EDS mapping spectra confirmed the presence of In, Cu, O, and C, respectively, consistent with the chemical composition in the In_2O_3/CuO-GNR photoanode.

In_2O_3/CuO-GNRs hybrid photoanodes were then tested in a typical three-electrode configuration with a Pt counter electrode and an Ag/AgCl reference electrode (saturated with 3 M KCl). N_2-purged 1 M NaOH aqueous solution (pH ≈ 13) was used as an electrolyte. All the PEC measurements were performed under dark, continuous, and chopped illumination (one sun illumination AM 1.5 G, 100mW cm^{-2}). Light-chopped linear sweep voltammetry (LSV) measurements on different

GNRs-In_2O_3/CuO photoanodes are reported in **Figure 5**. All the samples show low dark current densities, indicating that the photoanodes are almost inactive without light irradiation. On the contrary, the instant response of the photocurrent to the chopped illumination indicates an efficient separation of electron-hole pairs in the system induced by visible light. Figure 5g summarizes the variation of saturated photocurrent density values versus concentration of GNRs in the In_2O_3/CuO photoanode at 1.6 V RHE. The photocurrent density (J_{ph}) for all samples varies strongly with the change in the concentration of GNRs in In_2O_3/CuO composite. More in detail, the highest saturated J_{ph} of bare In_2O_3/CuO photoanode is 0.89 mA cm^{-2} (Figure 5a). By adding 0.01 wt% of GNRs in In_2O_3/CuO film, the J_{ph} increases to 0.98 mA cm^{-2} (Figure 5b), and reaches a maximum value of 1.51 mA cm^{-2} at 0.03 wt% of GNR content (Figure 5d), which is 70% higher than that of a PEC system based on a bare In_2O_3/CuO photoanode. Enhanced electron transport and reduced charge transfer resistance are mainly responsible for the increase in photocurrent density of In_2O_3/CuO-0.03 wt% GNRs photoanodes.[17b,20c]

The high electrical conductivity of the GNRs can provide a direct pathway to the photoinjected electrons towards the FTO, avoiding the numerous grain boundaries of In_2O_3/CuO composite, thereby enhancing electron collection.

If the concentration of GNRs is further increased, the J_{ph} diminishes from 1.51 to 1.04 mA cm^{-2} (0.04 wt%) (Figure 5e) and 0.66 mA cm^{-2} (0.05 wt%) (Figure 5f). This phenomenon is

Table 1. Band energies of CuO, In_2O_3, and In_2O_3/CuO nanocomposite calculated by UV-DRS, XPS, and UPS.

Sample	E_{BG} (eV)	E_F (eV)		E_{VBM} (eV)		E_{CBM} (eV)		ΔE_{VBO} (eV)	ΔE_{CBO} (eV)
		Vacuum	NHE	Vacuum	NHE	Vacuum	NHE		
CuO	1.79	−5.42	0.98	−5.62	1.18	−3.83	−0.61		
In_2O_3	2.70	−4.64	0.2	−6.75	2.31	−4.05	−0.39		
In_2O_3/CuO	2.24[a]	−4.01	−0.43	−5.90	1.46[b]	−3.66	−0.78[c]	1.03	0.12

[a]Apparent E_g; [b]The valence band maximum potential of In_2O_3 in In_2O_3/CuO nanocomposite; [c]The conduction band minimum potential of CuO in In_2O_3/CuO nanocomposite.

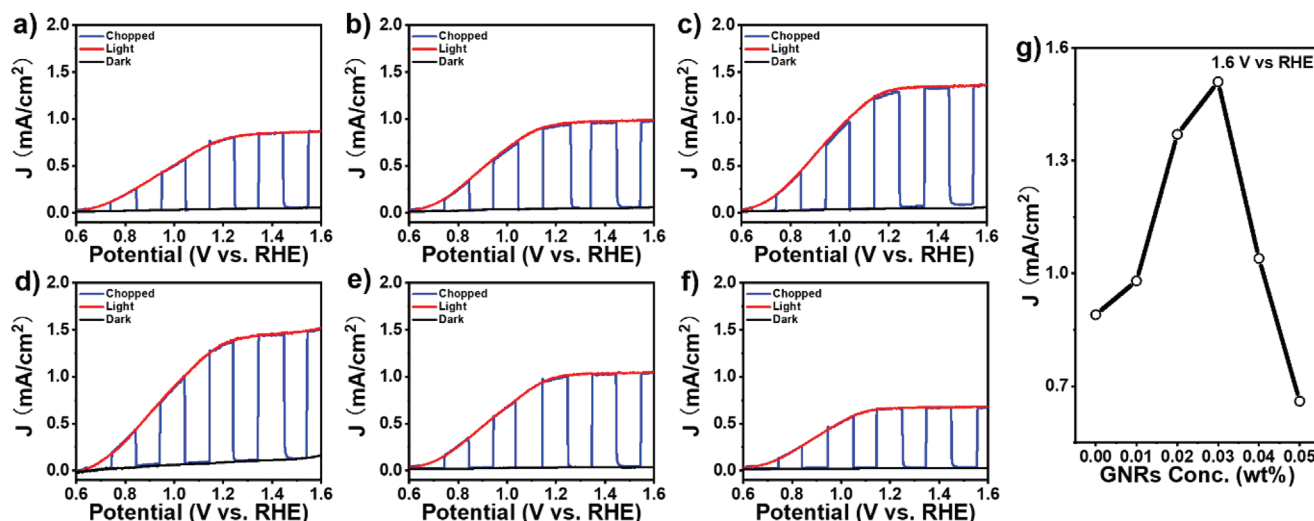**Figure 5.** Photocurrent density-potential curves of PEC devices based on In_2O_3/CuO-GNRs hybrid photoanodes with different concentrations of GNRs under dark, continuous, and chopped illumination (AM 1.5G, 100 mW cm^{-2}): a) 0.00 wt%; b) 0.01 wt%; c) 0.02 wt%; d) 0.03 wt%; e) 0.04 wt% and f) 0.05 wt%. g) Variation of current density at 1.6 V versus RHE under 100 mW cm^{-2} illumination with the concentration of GNRs.

mainly attributed to the negative effect (e.g., crack formation[17a]) of the high concentration of GNRs, which act as recombination centers during carrier transport, as well as to reduced optical transparency of the hybrid photoanode. Moreover, the small amount of GNRs (0.03 wt%) used does not affect the optical transparency of the film, as confirmed by UV-DRS tests (see Figure S6, Supporting Information).

To observe the influence of p-type CuO on the properties of the photoanode, the same experiment was also carried out by preparing a pure In_2O_3 film via MOF template method (see experiment part) under the same conditions. The J_{ph} of the pure In_2O_3 photocathode is only 0.3 mA cm^{-2} (Figure S12a, Supporting Information). In addition, after adding the same content (0.03 wt%) of GNRs in the In_2O_3 photocathode, the photocurrent density increases to 0.36 mA cm^{-2} (Figure S12b, Supporting Information), which is only 20% higher than that of a PEC system based on the bare In_2O_3 photoanode. However, if we compare the composite In_2O_3/CuO photoanode (0.89 mA cm^{-2}) with the bare In_2O_3 photoanode, the presence of CuO enhances the J_{ph} almost twofold. The comparative LSV plots of pure In_2O_3, In_2O_3/CuO, and In_2O_3/CuO-0.03 wt% GNRs are shown in **Figure 6**a and the chopped illumination data are also shown in Figure 6b. Overall, the J_{ph} of the optimized sample, In_2O_3/CuO-0.03 wt% GNRs, is ≈4. and 0.7-fold higher than those of pure In_2O_3 and In_2O_3/CuO, respectively. Such performance enhancement is attributed to the synergistic effect of the presence of a p-n junction due to the incorporation of CuO, which increases the charge separation at the interface and reduces recombination, and to the addition of an optimum amount of GNR, which can improve charge transport and collection inside the photoanode. The PEC performance of the In_2O_3/CuO-0.03 wt% GNRs obtained in this work compares favorably to those of representative In_2O_3 photocatalysts reported for PEC water splitting (Supporting Information, Table S2).

The long-term stability of the PEC device is a critical factor toward commercialization. In this work, the stability of

In_2O_3/CuO-0.03 wt% GNRs photoanode by chronoamperometry at 1.4 V versus RHE under AM 1.5 G solar illumination (100 mW cm^{-2}) (Figure 6d). The In_2O_3/CuO-0.03 wt% GNRs photoanode shows an obvious photocurrent density decrease in 0.5 M Na_2SO_4 (pH ≈ 6.8). However, when the electrolyte is substituted with an alkaline one (1 M NaOH, pH ≈ 13), the hybrid photoanode shows a remarkable stability for up to 5 h. As visible in Figure S13a,b, Supporting Information, the In_2O_3/CuO-0.03 wt% GNRs hollow hexagonal rod-shaped after the long-term operation retains its morphology.

To further investigate the mechanism behind the improved performance for different In_2O_3/CuO photoanodes on the carrier transport properties, electrochemical impedance spectroscopy (EIS) measurements were carried out. Figure 6c displays the Nyquist plots recorded at 1.4 V versus RHE under 1 Sun (100 mW cm^{-2}) of representative samples of In_2O_3, In_2O_3/CuO, and In_2O_3/CuO-0.03 wt% GNRs. To obtain information on the charge transport properties, the data were fitted with an equivalent circuit consisting of a series resistance (R_S) followed by two parallels of a space charge capacitance and resistance (C_{SC} and R_{SC}), double layer capacitance (C_{DL}), and charge transfer resistance (R_{CT}).). Similar models have been developed for related systems.[3,33] By extrapolating the R_{CT} for each device (Table S1, Supporting Information), a the optimum amount of GNRs in the In_2O_3/CuO composite shows the lowest R_{CT}, indicating a higher charge transfer and an improved separation of electron/hole pairs. In addition, compared to pure In_2O_3 and In_2O_3/CuO, the R_{CT} of In_2O_3/CuO is reduced. This could be due to a more favorable band alignment that allows faster charge transfer by the built-in electric field of the In_2O_3/CuO p-n heterojunction.

H_2 production was further measured during the chronoamperometric test for In_2O_3/CuO-0.03 wt% GNRs. The produced H_2 gas was detected using a gas chromatograph (GC) equipped with a thermal conductivity detector at 1.4 V versus RHE under 1 sun. Argon gas was used as the carrier gas for GC analysis. The evolution of H_2 exhibits a nearly linear increase
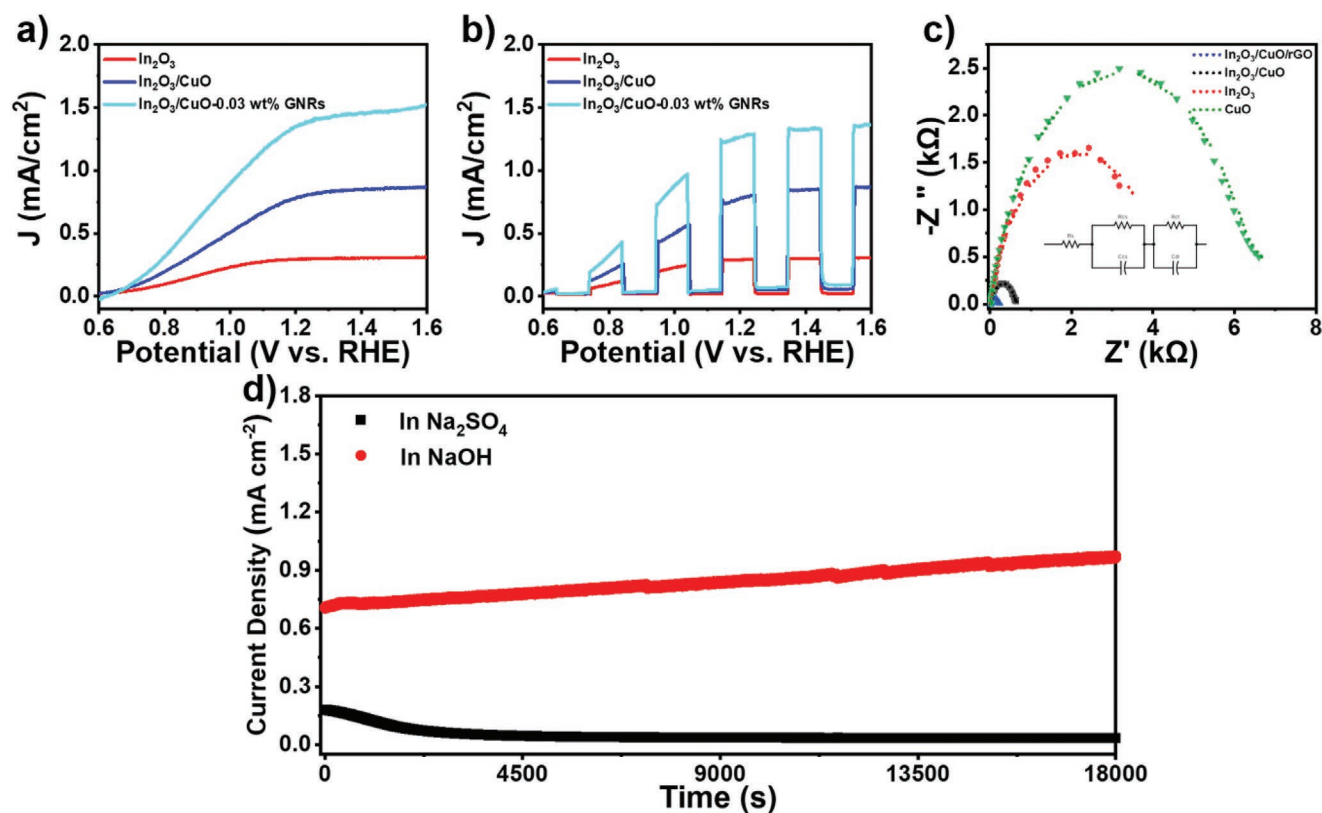
Figure 6. a) Comparative LSV curve of bare In_2O_3, In_2O_3/CuO, and In_2O_3/CuO-0.03 wt% GNRs. b) chopped illumination of bare In_2O_3, In_2O_3/CuO, and In_2O_3/CuO-0.03 wt% GNRs (Electrolyte 1 M NaOH). c) Nyquist plots of In_2O_3, In_2O_3/CuO composite, and In_2O_3/CuO-0.03 wt% GNRs (the inset is the equivalent circuit used for the fitting). d) Stability measurements (chronoamperometry) of In_2O_3/CuO-0.03 wt% GNRs in NaOH and Na_2SO_4 electrolyte, respectively (all experiments ran at 1.4 V versus RHE under AM 1.5 G illumination (100 mW cm^{-2})).

over time (solid red curve) (Figure S14, Supporting Information). The evolution is also calculated from the measured current (solid black curve). The associated Faradaic efficiencies ($\eta_{Faradaic}$)(95.11%) are determined by comparing the amount of gas produced experimentally with the theoretically calculated values (Detailed calculations are provided in the Supporting information). The difference between the measured and calculated value of H_2 might be due to gas leakage in our homemade prototype experimental system.

3. Conclusions

In summary, In_2O_3/CuO hollow hexagonal rod-shaped has been successfully developed via MOF-templating. Structural investigations confirmed that, after the annealing process, the In_2O_3/CuO retained the MOF morphology. To improve the efficiency of the In_2O_3/CuO photoanode for PEC H_2 generation, a controlled amount of GNRs can be incorporated in the film. By forming a p-n heterojunction, the In_2O_3/CuO-photoanode showed a 2-fold enhanced current density compared to the pure In_2O_3-phtoanode. This is mainly attributed to the improved separation efficiency of photogenerated electron-hole pairs in the In_2O_3/CuO-photoanode. Further, by adding an optimized concentration of GNRs (0.03 wt%) in the In_2O_3/CuO-hybrid, the photocurrent density can be boosted to 1.51 mA cm^{-2}, which

is 70% higher than the In_2O_3/CuO photoanodes. This value is also higher than the photocurrent density reported for the PEC performance of previous representative In_2O_3 photocatalysts. As confirmed by our analysis, an optimum GNRs concentration in the In_2O_3/CuO-photoanode can improve the electrons transport by reducing the R_{ct}, without altering the optical/structural properties of the photoanode. Overall, these findings provide fundamental insights into MOF-derived metal oxides nanostructures, indicating that this type of material can deliver promising performance in terms of stability and photocurrents as photoelectrode materials for PEC hydrogen production. While there are still many challenges ahead before they can be widely commercialized in PEC water splitting, it is anticipated that the results reported here will inspire further research in this area, leading to novel and improved MOF architectures for applications in energy conversion.

4. Experimental Section

Materials and Chemicals: *N,N*-Dimethylformamide (DMF), indium(III) nitrate hydrate ($In(NO_3)_3 \cdot xH_2O$), copper(II) nitrate trihydrate ($Cu(NO_3)_2$ $3H_2O$), 1,4-benzenedicarboxylic acid (H_2BDC), sodium hydroxide (NaOH), graphene nanoribbons (GNRs) of several micrometers length and below 100 nm width, ethyl cellulose, alpha-terpineol, acetone, methanol, ethanol, and sodium sulfate (Na_2SO_4) were purchased from Sigma–Aldrich Inc. Fluorine doped tin oxide (FTO) coated glass

substrates with sheet resistance 10 Ω/square were bought from South China Xiang Science & Technology Company Limited. All chemicals were used as received, without further purification.

Synthesis of MIL-68(In)-MOFs Hexagonal Rod Precursor: A modified version of MIL-68(In) was prepared according to previous work.[34] Typically, a mixture milky solution was prepared by mixing 1,4-benzenedicarboxylic acid (H_2BDC, 0.4 mol, 32 mg) and $In(NO_3)_3$ xH_2O (0.4 mol, 7.8 mg) in 18 mL of DMF. Afterward, the mixture was heated in an oil bath (100 °C) for 15 min. Upon cooling down, the final white products were centrifuged and washed with DMF and methanol three times, respectively. The collected materials were then dried in an oven overnight at 80 °C.

Synthesis of Cu-BDC Precursor: A 96.8 (0.4 mol) mg of the $Cu(NO_3)_2$ $3H_2O$ and 32 mg (0.4 mol) H_2BDC were dissolved in 18 mL DMF. The resulting mixture was placed in an oil bath (100 °C) for 10 min. Light blue Cu-BDC generated in this time were isolated by cooling the reaction mixture to room temperature, collecting the precipitate by centrifugation, and washing three times with DMF and methanol. The collected materials were then dried in an oven overnight at 80 °C.

Synthesis of MIL-68(In)/Cu-BDC Hexagonal Rods Precursor: A 100 mg of the obtained MIL-68(In) hexagonal rod powders, and 96.8 mg (0.4 mol) of $Cu(NO_3)_2$ $3H_2O$ were dispersed in 18 mL DMF. After stirring continuously at room temperature for 30 min, the mixture was heated in an oil bath (100 °C) for 15 min. After cooling down, the final products were centrifuged and washed with DMF and methanol three times, respectively. The collected materials were then dried in an oven overnight at 80°C.

Synthesis of Pure In_2O_3: A 0.5 g of the MIL-68(In) powder was annealed in a tube furnace in air atmosphere to 500 °C with a ramp-rate of 5 °C/min and held for 60 min. After natural cooling, white powders of pure In_2O_3 were obtained.

Synthesis of Pure CuO: A 0.5 g of the Cu-BDC powder was annealed in a tube furnace in ambient air to 350 °C with a ramp-rate of 5 °C/min and held for 60 min. After naturally cooling, black powders of pure CuO were obtained.

Synthesis of In_2O_3/CuO Nanocomposite: A 0.5 g of the MIL-68(In)/Cu-BDC hexagonal rods precursor powder was annealed in a tube furnace in ambient air to 500 °C with a ramp-rate of 5 °C/min and held for 60 min. After natural cooling, light brown powders of In_2O_3/CuO were obtained.

Preparation of In_2O_3, CuO and In_2O_3/CuO Paste: A 0.2 g corresponding products were mixed with 0.5 ml ethanol as a solvent, 0.2 ml alpha-terpineol as dispersant, 0.1 g ethyl cellulose which acts as a thickener, and 0.2 ml of water. The mixture solution was transferred into a beaker and stirred overnight. The solvent was removed by connecting it to a vacuum pump during continuous magnetic stirring until the volume of the mixture was reduced to half of the starting volume.

Fabrication of the In_2O_3/CuO Photoanode: Fluorine-doped tin oxide (FTO) glass substrates were cleaned ultrasonically for 15 min with ethanol, then rinsed in deionized (DI) water and dried in N_2 gaseous flow. The cleaned FTO glass substrates were then treated in a UV-ozone cleaner for 10 min to further eliminate surface organic contaminants. Successively, a pure In_2O_3 layer was deposited onto FTO substrates using the doctor blade technique and kept in air for 12 min to completely spread out. The electrodes were subsequently dried at 120 °C for 6 min. A second layer of In_2O_3/CuO paste was then deposited on the top, following the same procedure. The photoanodes were later sintered at 500 °C for 30 min in a furnace and cooled down to obtain the different photoanodes.

Fabrication of the In_2O_3/CuO-GNRs Photoanode: A dispersion of graphene nanoribbons (GNRs) in ethanol was prepared by mixing 4 mg of GNRs in 10 mL of ethanol and sonicated for 6 h. In_2O_3/CuO-GNRs hybrid pastes with different concentration of GNRs were prepared by mixing a precise amount of ethanolic suspension of GNRs into a known weight of In_2O_3/CuO paste. The electrode was fabricated with similar procedures except that for the first layer paste we used In_2O_3-GNRs instead of pure In_2O_3 paste and for the second layer paste we used In_2O_3/CuO-GNRs instead of In_2O_3/CuO paste.

Fabrication of the In_2O_3 Photoanode: The In_2O_3 electrode was fabricated with similar procedures as those used for the fabrication of the In_2O_3/CuO photoanode electrode except that In_2O_3 was used as second layer paste instead of In_2O_3/CuO paste.

Characterization: The crystal structure of the obtained products was characterized by X-ray diffraction using a Bruker D8 X-ray diffractometer with Cu-K_α radiation (λ = 1.54178 Å). High-resolution transmission electron microscopy (HRTEM) images and EDS were collected by using a JEOL 2100F TEM and an Xplore model. SEM was collected by Tescan LYRA 3 XMH. TGA was obtained via Thermogravimetric Analyzer (Q500). X-ray photoelectron spectroscopy (XPS) was performed in a VG Escalab 220i-XL equipped with hemispherical analyzer, applying a twin anode X-ray source, calibrated using carbon at 284.8 eV. The same deconvolution procedure was applied throughout the analysis of the peaks and basically involves the subtraction of a Tougaard -type baseline and the use of Voigt-type functions to reproduce the spectra. Ultraviolet photoelectron spectroscopy (UPS) data was obtained with HeI (21.21 eV) as monochromatic light source. UV-vis diffuse reflectance spectra (DRS) were obtained using an UV-vis spectrometer (Cary 5000). The produced H_2 gas was detected using a gas chromatograph (GC) (Perkin Elmer Clarus 580 GC) equipped with a thermal conductivity detector. Argon gas was used as the carrier gas for GC analysis. An air-tight syringe was used for sampling from the vacuum-sealed chamber. The Raman spectra of the photoanode were recorded using a Renishaw InVia spectrometer coupled with a 514 nm excitation source.

Evaluation of PEC Performance: A Gamry 1000E electrochemical workstation was employed to test the electrochemical measurements and the following formula $V_{RHE} = V_{Ag/AgCl} + 0.1976 + pH \times (0.059)$ was used to convert the measured potentials (vs Ag/AgCl) to the potentials with respect to the RHE. Photocurrent density–voltage (J–V) curves were obtained by linear sweep voltammetry (LSV, with sweep rate of 20 mV s^{-1}) and by a Compact Solar Simulator Class AAA (Sciencetech SLB-300A) with a 150 W Xenon lamp as light source with an AM 1.5G filter at 1 sunlight intensity (100 mW cm^{-2}). All the samples were back-illuminated (from the FTO glass side). Prior to each measurement, a Si reference diode (Sciencetech) was used to adjust the distance between photocathode and solar simulator to guarantee the standard 1 sun illumination (100 mW cm^{-2}) on the photocathode in our three-electrode system. The distance from sun simulator to PEC cell was fixed at 15 cm. Electrochemical impedance spectroscopy (EIS) was carried out at 0.9 V versus RHE under 1 Sun (100 mW cm^{-2}) by using a Gamry 1000E electrochemical workstation. All impedance measurements were analyzed using an appropriate equivalent circuit model with Z-View software (v3.5, Scribner Associate, Inc.).

Supporting Information

Supporting Information is available from the Wiley Online Library or from the author.

Acknowledgements

[1] a) Y. Yang, S. Niu, D. Han, T. Liu, G. Wang, Y. Li, *Adv. Energy Mater.* **2017**, *7*, 1700555; b) I. Concina, Z. H. Ibupoto, A. Vomiero, *Adv. Energy Mater.* **2017**, *7*, 1700706.

[2] A. Sartbaeva, V. Kuznetsov, S. Wells, P. Edwards, *Energy Environ. Sci.* **2008**, *1*, 79.

[3] L. Shi, D. Benetti, F. Li, Q. Wei, F. Rosei, *Appl. Catal. B* **2020**, *263*, 118317.

[4] P. Zhang, X. F. Lu, D. Luan, X. W. Lou, *Angew. Chem., Int. Ed.* **2020**, *132*, 8205.

[5] a) H. Li, C. Chen, X. Huang, Y. Leng, M. Hou, X. Xiao, J. Bao, J. You, W. Zhang, Y. Wang, *J. Power Sources* **2014**, *247*, 915; b) E. Cao, G. Song, Z. Guo, Y. Zhang, W. Hao, L. Sun, Z. Nie, *Mater. Lett.* **2020**, *261*, 126985.

[6] H. Xu, H. Chen, S. Chen, K. Wang, X. Wang, *Int. J. Hydrogen Energy* **2021**, *46*, 32445.

[7] a) X. Zhang, Y. Liu, Z. Kang, *ACS Appl. Mater. Interfaces* **2014**, *6*, 4480; b) T. Zhou, J. Wang, S. Chen, J. Bai, J. Li, Y. Zhang, L. Li, L. Xia, M. Rahim, Q. Xu, *Appl. Catal. B* **2020**, *267*, 118599; c) W. Hamd, M. Chavarot-Kerlidou, J. Fize, G. Muller, A. Leyris, M. Matheron, E. Courtin, M. Fontecave, C. Sanchez, V. Artero, *J. Mater. Chem. A* **2013**, *1*, 8217; d) S.-S. Yi, Z.-Y. Wang, H.-M. Li, Z. Zafar, Z.-T. Zhang, L.-Y. Zhang, D.-L. Chen, Z.-Y. Liu, X.-Z. Yue, *Appl. Catal. B* **2021**, *283*, 119649.

[8] L. Sun, Y. Zhuang, Y. Yuan, W. Zhan, X. J. Wang, X. Han, Y. Zhao, *Adv. Energy Mater.* **2019**, *9*, 1902839.

[9] a) M. Kibria, F. Chowdhury, S. Zhao, B. AlOtaibi, M. Trudeau, H. Guo, Z. Mi, *Nat. Commun.* **2015**, *6*, 6797; b) J. L. Young, K. X. Steirer, M. J. Dzara, J. A. Turner, T. G. Deutsch, *J. Mater. Chem. A* **2016**, *4*, 2831; c) M. H. Lee, K. Takei, J. Zhang, R. Kapadia, M. Zheng, Y. Z. Chen, J. Nah, T. S. Matthews, Y. L. Chueh, J. W. Ager, *Angew. Chem., Int. Ed.* **2012**, *51*, 10760; d) B. Liu, X.-B. Li, Y.-J. Gao, Z.-J. Li, Q.-Y. Meng, C.-H. Tung, L.-Z. Wu, *Energy Environ. Sci.* **2015**, *8*, 1443.

[10] a) Z. Lin, J. Xiao, L. Li, P. Liu, C. Wang, G. Yang, *Adv. Energy Mater.* **2016**, *6*, 1501865; b) J. F. de Brito, F. Tavella, C. Genovese, C. Ampelli, M. V. B. Zanoni, G. Centi, S. Perathoner, *Appl. Catal., B* **2018**, *224*, 136.

[11] a) S. Velmurugan, T. C.-K. Yang, J.-N. Chen, L. Zhi-Xiang, *Microchim. Acta* **2021**, *188*, 372; b) X. Liang, T.-H. Kim, J.-W. Yoon, C.-H. Kwak, J.-H. Lee, *Sens. Actuators, B* **2015**, *209*, 934.

[12] R. R. Salunkhe, Y. V. Kaneti, Y. Yamauchi, *ACS Nano* **2017**, *11*, 5293.

[13] H. Chen, Y. Zhou, W. Guo, B. Y. Xia, *Chin. Chem. Lett.* **2022**, *33*, 1831.

[14] Y. V. Kaneti, J. Tang, R. R. Salunkhe, X. Jiang, A. Yu, K. C. W. Wu, Y. Yamauchi, *Adv. Mater.* **2017**, *29*, 1604898.

[15] Y. Yang, L. Sun, W. Zhan, X. Wang, X. Han, *J. Mater. Chem. A* **2021**, *9*, 4310.

[16] a) D. Benetti, F. Rosei, in *Halide Perovskites for Photonics*, AIP Publishing LLC Melville, New York **2021**, p. 4; b) M. Batmunkh, M. J. Biggs, J. G. Shapter, *Small* **2015**, *11*, 2963.

[17] a) G. S. Selopal, M. Mohammadnezhad, F. Navarro-Pardo, F. Vidal, H. Zhao, Z. M. Wang, F. Rosei, *Nanoscale Horiz.* **2019**, *4*, 404; b) D. Benetti, K. T. Dembele, J. Benavides, H. Zhao, S. Cloutier, I. Concina, A. Vomiero, F. Rosei, *J. Mater. Chem. C* **2016**, *4*, 3555.

[18] K. T. Dembele, G. S. Selopal, R. Milan, C. Trudeau, D. Benetti, A. Soudi, M. M. Natile, G. Sberveglieri, S. Cloutier, I. Concina, *J. Mater. Chem. A* **2015**, *3*, 2580.

[19] Z. Yin, S. Wu, X. Zhou, X. Huang, Q. Zhang, F. Boey, H. Zhang, *Small* **2010**, *6*, 307.

[20] a) X. Meng, C. Yu, X. Song, Y. Liu, S. Liang, Z. Liu, C. Hao, J. Qiu, *Adv. Energy Mater.* **2015**, *5*, 1500180; b) N. Mohanty, D. Moore, Z. Xu, T. Sreeprasad, A. Nagaraja, A. A. Rodriguez, V. Berry, *Nat. Commun.* **2012**, *3*, 844; c) R. Akilimali, G. S. Selopal, D. Benetti, I. Serrano-Esparza, P. A. Algarabel, J. M. De Teresa, Z. M. Wang, B. Stansfield, H. Zhao, F. Rosei, *J. Power Sources* **2018**, *396*, 566.

[21] W. Guo, X. Sun, C. Chen, D. Yang, L. Lu, Y. Yang, B. Han, *Green Chem.* **2019**, *21*, 503.

[22] a) N. Bouazizi, R. Bargougui, A. Oueslati, R. Benslama, *Adv. Mater. Lett.* **2015**, *6*, 158; b) K. N. Fatema, S. Sagadevan, Y. Liu, K. Y. Cho, C.-H. Jung, W.-C. Oh, *J. Mater. Sci.* **2020**, *55*, 13085.

[23] X. Tong, Y. Zhou, L. Jin, K. Basu, R. Adhikari, G. S. Selopal, H. Zhao, S. Sun, A. Vomiero, Z. M. Wang, *Nano Energy* **2017**, *31*, 441.

[24] Y. Yang, D. Xu, Q. Wu, P. Diao, *Sci. Rep.* **2016**, *6*, 35158.

[25] R. Marschall, *Adv. Energy Mater.* **2014**, *24*, 2421.

[26] C. He, Q. Liu, H. Wang, C. Xia, F. M. Li, W. Guo, B. Y. Xia, *Small* **2023**, 2207474.

[27] M. E. Aguirre, R. Zhou, A. J. Eugene, M. I. Guzman, M. A. Grela, *Appl. Catal. B* **2017**, *217*, 485.

[28] E. Kraut, R. Grant, J. Waldrop, S. Kowalczyk, *Phys. Rev. Lett.* **1980**, *44*, 1620.

[29] B. L. Sharma, R. K. Purohit, *Semiconductor Heterojunctions*, Vol. 5, Elsevier, **2015**.

[30] G. M. Kumar, A. M. Kumar, P. Ilanchezhiyan, T. Kang, *Nanoscale* **2014**, *6*, 11226.

[31] a) H. Guo, C.-G. Niu, D.-W. Huang, N. Tang, C. Liang, L. Zhang, X.-J. Wen, Y. Yang, W.-J. Wang, G.-M. Zeng, *Chem. Eng. J.* **2019**, *360*, 349; b) S. Li, J. Pan, H. Li, Y. Liu, W. Ou, J. Wang, C. Song, W. Zhao, Y. Zheng, C. Li, *Chem. Eng. J.* **2019**, *366*, 305.

[32] S. Jovanović, T. Da Ross, A. Ostric, D. Tošić, J. Prekodravac, Z. Marković, B. T. Marković, *Phys. Scr.* **2014**, *2014*, 014023.

[33] S. Hernández, D. Hidalgo, A. Sacco, A. Chiodoni, A. Lamberti, V. Cauda, E. Tresso, G. Saracco, *Phys. Chem. Chem. Phys.* **2015**, *17*, 7775.

[34] W. Cho, H. J. Lee, M. Oh, *J. Am. Chem. Soc.* **2008**, *130*, 16943.